nature chemical engineering

Article

https://doi.org/10.1038/s44286-024-00102-9

Engineering and direct imaging of nanocube self-assembly pathways

Received: 5 December 2023

Accepted: 1 July 2024

Yaxu Zhong[1,4], Timothy C. Moore[2,4], Tobias Dwyer[2,4], Alex Butrum-Griffith[1], Vincent R. Allen[1], Jun Chen[1], Yi Wang[1], Fanrui Cheng[1], Sharon C. Glotzer[2,3] & Xingchen Ye[1]

Nanoparticle self-assembly offers a scalable and versatile means to fabricate next-generation materials. The prevalence of metastable and nonequilibrium states during the assembly process makes the final structure and function directly dependent upon formation pathways. However, it remains challenging to steer the assembly pathway of a nanoparticle system toward multiple superstructures while visualizing in situ. Here we use liquid-cell transmission electron microscopy to image complete self-assembly processes of gold nanocubes, a model shape-anisotropic nanocolloidal system, into distinct superlattices. Theoretical analysis and molecular dynamics simulations indicate that the electrostatic screening of the medium dictates self-assembly pathways by its effects on the interactions between nanocubes. We leverage this understanding to demonstrate on-the-fly control of assembly behavior through rapid solvent exchange. Our joint experiment–simulation–theory investigation paves the way for elucidating the relationships among building block attributes, assembly pathways and superstructures in nanoscale assembly and opens new avenues for the bottom-up design of reconfigurable and adaptive metamaterials.

Fluid–solid and solid–solid transitions are central to the formation of natural and synthetic materials spanning many length scales. Examples include the crystallization of ice[1] and proteins[2], the formation of metal alloys[3], biomineralization[4], and self-assembly of nanoparticles[5] and micrometer-sized colloids[6] into ordered phases. With nanoscale building blocks, the ever-increasing structural diversity, complexity and reconfigurability of their self-organized superstructures promise to open new doors to developing next-generation functional materials and devices[7–21]. Understanding the mechanisms and pathways underlying ordering transitions is necessary to provide design guidelines for targeted structures and to refine existing models of phase transitions in atomic and colloidal systems. In comparison with predicting the final structures, forecasting ordering pathways from building block attributes such as shape anisotropy is far more difficult, even when the pairwise interactions are known. This difficulty arises from emergent phenomena in ensembles of nanoparticles, for example, nonadditive interactions[22,23], prenucleation motifs[24,25] and multistep nucleation[26–30]. A critical first step in understanding building-block–pathway–superstructure relationships is direct observation of kinetic pathways from the appearance of the first crystalline nuclei to the equilibrium or steady-state superstructure. Optical microscopy has been widely used to directly visualize the dynamics of micrometer-scale colloids[31–35]; however, limited studies have demonstrated in situ imaging of nanoparticle assembly owing to the experimental challenges in controllably initiating and capturing ordering processes with single-particle resolution[29,30].

Here, using liquid-cell transmission electron microscopy (LCTEM)—an increasingly valuable technique for studying nanoscale dynamics of materials in their native environments[29,30,36–46]—we imaged the entire self-assembly pathways of gold nanocubes (AuNCs), a model shape-anisotropic nanocolloidal system, into diverse two-dimensional

---

[1]Department of Chemistry, Indiana University, Bloomington, IN, USA. [2]Department of Chemical Engineering, University of Michigan, Ann Arbor, MI, USA. [3]Biointerfaces Institute, University of Michigan, Ann Arbor, MI, USA. [4]These authors contributed equally: Yaxu Zhong, Timothy C. Moore, Tobias Dwyer. e-mail: sglotzer@umich.edu; xingchen@iu.edu

https://doi.org/10.1038/s44286-024-00102-9

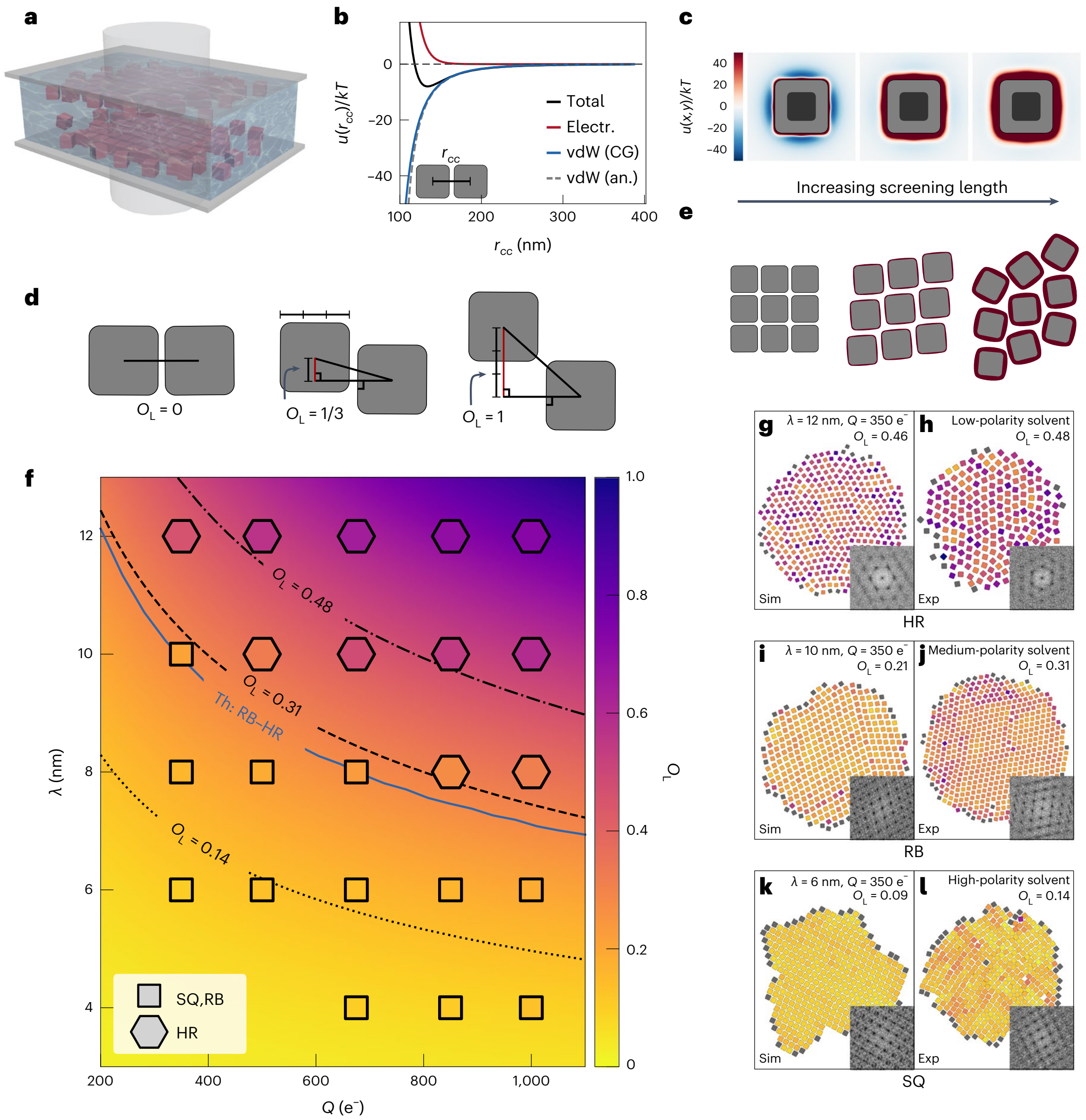

Fig. 1 | Charge screening controls the self-assembly phase behavior of gold nanocubes. a, LCTEM schematic showing the self-assembly of AuNCs near the Si_3N_4 windows under electron beam irradiation (gray cylinder) in organic solvent. **b**, Pairwise interaction potentials as a function of the center-to-center distance r_{CC} between AuNCs aligned face-to-face (schematic in inset), as used in the CG model (solid lines) or calculated from analytical theory (dashed line). Electr., electrostatic; an., analytical theory. **c**, Interaction potential fields $u(x, y)$ for a pair of parallel-aligned Au nanocubes assuming a total charge of 350 e⁻ per nanocube and screening lengths of 6 nm, 10 nm and 12 nm from left to right. The dark squares at the centers represent a single nanocube, whereas the lighter squares represent the excluded volume between the nanocubes. **d**, Schematic of the offset order parameter O_L used to characterize how square-like a lattice is. **e**, Schematics of the 2D superlattices observed experimentally. From left to right: SQ, RB and HR phases, corresponding to the $u(x, y)$ in **c**. **f**, Theoretical phase diagram as a function of charge per nanocube (Q) and electrostatic screening length (λ). The background colors denote predicted phases characterized by O_L from the scaling theory, and the markers indicate structures observed in simulations at each (Q, λ) pair, colored by O_L. The black lines are contours of constant O_L that match the experimentally observed O_L for each lattice type. The blue line is the predicted loci of the RB-to-HR structural transition. **g**–**l**, Snapshots from simulations (**g**, **i** and **k**) and LCTEM experiments (**h**, **j** and **l**) with particles colored according to O_L with the same color map as in **f**. Gray particles have fewer than three nearest neighbors and were excluded from the O_L calculation. The insets are fast Fourier transform (FFT) patterns of a subregion of the image to highlight the symmetry of a single-crystalline grain. Simulation parameters (solvent conditions) are indicated above each simulation (experimental) snapshot. Sim, simulation; Exp, experiment.

(2D) superlattices. The dominant forces between AuNCs in solution include van der Waals (vdW) attractions and screened electrostatic repulsions given that AuNCs typically become charged under LCTEM imaging conditions (Fig. 1a)[30,47–49]. Previous work demonstrated that the electrostatic repulsion between nanoparticles decreases with increasing solvent polarity under LCTEM illumination, plausibly caused by higher ionic strength (resulting in a smaller screening length) from solvent radiolysis[30]. Based on this observation and the fact that the solvent changes the vdW attractions to a negligible extent, we hypothesized that we can fine-tune the interaction potential between AuNCs and, hence, engineer their assembly behavior by varying the solvent. We performed molecular dynamics (MD) simulations of AuNC assembly explicitly accounting for these interactions and developed a scaling theory to show that the electrostatic screening controls the

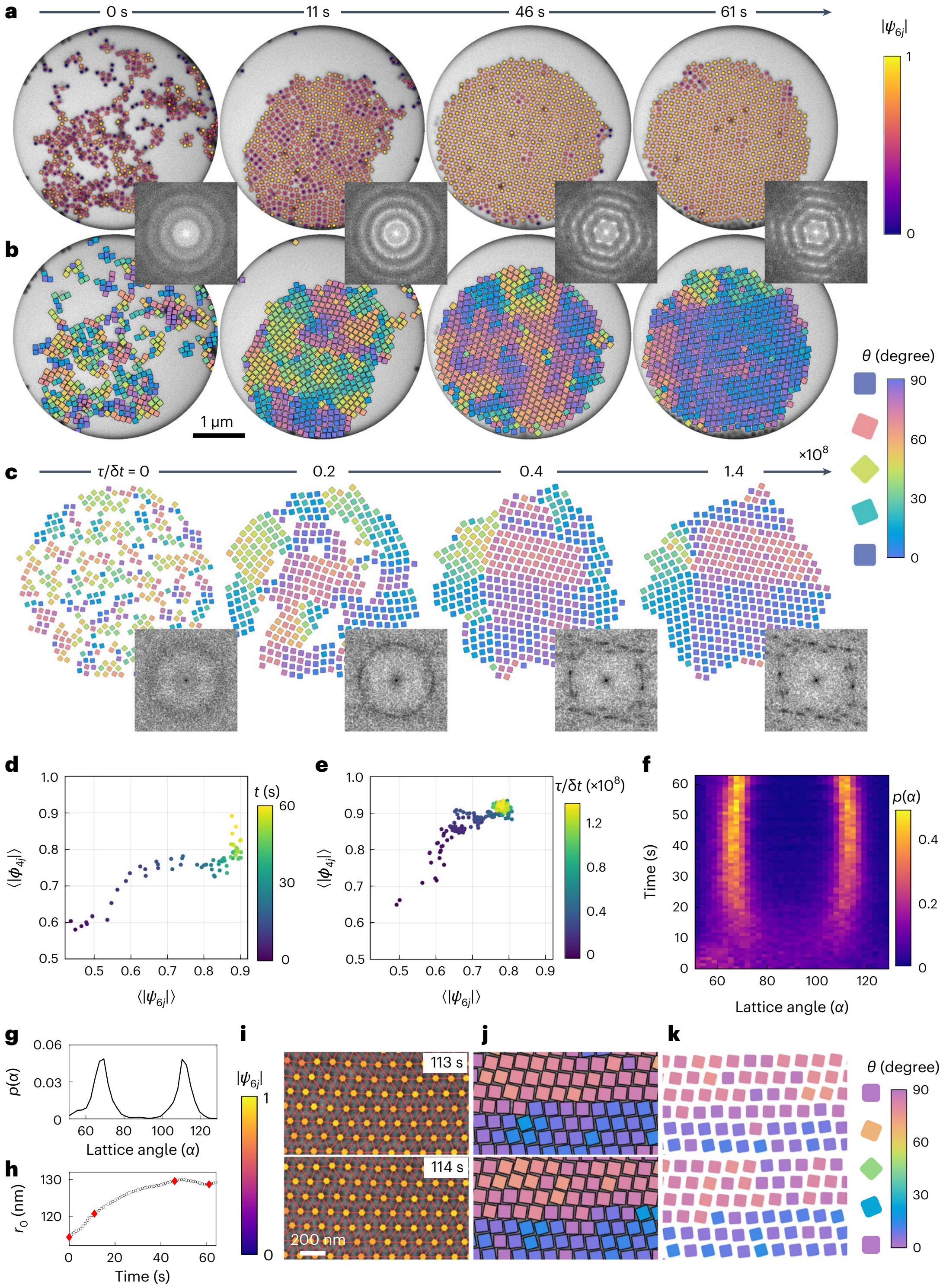

Fig. 2 | Self-assembly pathway of gold nanocubes into the RB lattice. **a**,**b**, Time-lapse LCTEM images and corresponding FFT patterns with nanocube centroids colored according to the modulus of sixfold bond-orientational order parameter ($|\psi_{6j}|$) and all nearest-neighbors connected (**a**), and nanocubes colored according to their orientations (**b**). **c**, Simulation snapshots and corresponding FFT patterns for the disorder-to-order transition of AuNCs into the RB lattice. **d**,**e**, Plots of averaged local translational and orientational order parameters ($\langle|\psi_{6j}|\rangle$, $\langle|\phi_{4j}|\rangle$) versus time for experimental LCTEM (**d**) and simulation (**e**) trajectories. **f**, Time-dependent lattice angle distribution from LCTEM experiment. **g**, Plot of lattice angle distribution of the RB phase at t = 61 s. **h**, Plot of nearest-neighbor distance retrieved from the first peak of $g(r)$ versus time. The red dots highlight the four stages shown in **a** and **b**. **i**–**k**, Movement of twin boundary through collective particle rotations in a nanocube superlattice. LCTEM images with nanocube centroids colored according to $|\psi_{6j}|$ (**i**). LCTEM images (**j**) and simulation snapshots (**k**) with nanocubes colored according to their orientations.

assembly behavior of these nanocubes. We quantified the pathways by analyzing the development of lattice translational order and particle orientational order during the assembly of AuNCs with solvent-tuned interparticle interactions, ranging from weakly to strongly attractive. Finally, we elucidated the pathways of superlattice melting and symmetry transitions, both induced by rapid solvent exchange.

Results

Theory and simulations of gold nanocube self-assembly

We developed a coarse-grained (CG) model to calculate the pairwise interactions between AuNCs (Supplementary Note 1 and Supplementary Fig. 1). We simulated systems over a range of electrostatic screening length (λ) and total charge (Q) based on estimates from our previous study[30]. As shown in Fig. 1b,c and Supplementary Fig. 2, the maximum overall attraction between AuNCs falls in the range of 5–40 kT. The interaction field becomes more isotropic and the effective particle size increases (considering a contour of zero potential) with increasing λ (Fig. 1c). Three ordered phases self-assembled from initial disorder in simulations, namely square-like (SQ), rhombic (RB) and hexagonal rotator (HR) phases, with increasing Q and λ (Fig. 1e,f and Supplementary Movies 1–3). We defined an offset-length order parameter O_L to quantify the extent to which these superlattices deviate from a perfect square lattice (Fig. 1d). With decreasing overall attraction (that is, increasing Q and λ), we observed increasing O_L values concomitant with the SQ-to-RB-to-HR symmetry transitions (Fig. 1f–l). These simulation results were insensitive to the charge distribution on the AuNCs (Supplementary Note 2 and Supplementary Fig. 3), suggesting that the predicted phase behavior is robust toward modest changes in the form of electrostatic repulsion between AuNCs. Moreover, we found the $O_L(Q, \lambda)$ relationships predicted by simulation collapse onto a master curve within a scaling theory (Supplementary Note 3 and Supplementary Fig. 3); this convergence indicates a universal relationship between interparticle interactions and the observed phase behavior. The scaling theory additionally enables identification of (Q, λ) pairs that yield the experimentally observed O_L values (Fig. 1f, black lines). Notably, there are no λ values that yield all three experimental O_L values across the range of Q studied, whereas all experimental O_L values are accessible by changing λ for $Q \geq 350\ e^-$, suggesting that λ is the more relevant control variable of self-assembly behavior. Further, the stability limit of the HR phase can be estimated by assuming that it can be stable only when the center-to-center distance between AuNCs that minimizes the interaction potential ($r_{\min}$) is such that AuNCs can rotate freely without colliding with nearest neighbors ($r_{\min} > r^*$); we take r^* to be the sum of λ and the AuNC circumsphere diameter (Supplementary Note 4). Above (below) this stability limit (Fig. 1f, blue line), the HR phase is accessible (inaccessible) across the entire range of Q examined.

Direct imaging and pathway analysis of gold nanocube self-assembly

We imaged the assembly process of polymer-grafted AuNCs into 2D superlattices in nonaqueous media using LCTEM (Fig. 1a). AuNCs (edge length $L_c = 87.4 \pm 3.2$ nm; Supplementary Fig. 4 and Supplementary Note 5) were densely grafted with thiol-terminated polystyrene (molecular weight $M_w = 3.2$ kDa) via ligand exchange to prevent uncontrolled aggregation under LCTEM conditions. The AuNCs became immobilized on the Si_3N_4 windows before transmission electron microscopy (TEM) imaging but began to move within seconds of electron beam illumination. The increased mobility is plausibly caused by positive charging of the AuNCs via contact electrification[47] or emission of Auger and secondary electrons[48–50] and positive charging of the Si_3N_4 windows[30,47,51,52]. With decreasing solvent polarity (butanol, 1:1 v/v octane/butanol and 4:1 v/v octane/butanol), we observed the formation of SQ, RB and HR phases, respectively, as indicated visually and by the fast Fourier transform (FFT) patterns of the TEM images, consistent with simulations at $\lambda = 6$, 10 and 12 nm with $Q = 350\ e^-$ (Fig. 1g–l). We also observed an increasing O_L with decreasing solvent polarity, analogous to the trend of increasing O_L with increasing screening length in simulations. The perimeters of the RB and HR phases are more dynamic than in the SQ phase, indicative of weaker net interparticle attraction in less polar solvents (cf. Supplementary Movies 4, 6 and 7). These computational and experimental results demonstrate that the interplay between vdW and electrostatic forces mediated by solvent polarity dictates the self-assembly phase behaviors of AuNCs. Our LCTEM imaging also allowed us to rule out interactions between polymer brushes as a driver of the self-assembly behaviors (Supplementary Notes 6 and 7).

Beyond characterizing the final structures, our LCTEM workflow enabled imaging and analysis of the full assembly pathways of AuNCs into superlattices (Supplementary Notes 8–10 and Supplementary Figs. 5–7). Figure 2a and Supplementary Movie 4 illustrate the four key stages during the formation of the RB phase. At 0 s, AuNCs were sparsely distributed within the field of view and exhibited low sixfold bond-orientational order ($\langle|\psi_{6j}|\rangle < 0.5$). The absence of long-range translational symmetry and AuNC orientational order were manifested by the diffuse rings of the corresponding FFT pattern and orientation plot (Fig. 2b), respectively. At 11 s, small hexagonally ordered domains exhibiting local facet alignment emerged. These domains were separated by disordered regions causing a lack of global translational order as shown by the FFT pattern. At 46 s, an extended 2D superlattice appeared. Despite its high sixfold bond-orientational order ($\langle|\psi_{6j}|\rangle > 0.7$), the corresponding AuNC orientation map revealed differently oriented domains each characterized by extensive facet alignment. At 61 s, a large coherent superlattice with extensive facet alignment had formed.

The evolution of the translational symmetry and orientational order during RB superlattice formation reveals an intriguing assembly pathway (Fig. 2d). From 0 to 11 s, both order parameters increased rapidly as individual AuNCs coalesced into a polycrystalline structure with short-range order. From 11 to 46 s, $\langle|\psi_{6j}|\rangle$ continually increased and the distribution of $|\psi_{6j}|$ narrowed drastically, whereas $\langle|\phi_{4j}|\rangle$ remained essentially constant and broadly distributed (Fig. 2d and Supplementary Fig. 8). These results indicate that the development of long-range translational order preceded extensive orientational order as the system eliminated grain boundaries and grew by adding AuNCs into the existing lattice. From 46 to 61 s, $\langle|\phi_{4j}|\rangle$ rose sharply. In essence, the rotational ordering of AuNCs through facet alignment induced a hexagonal-to-RB lattice transition. Such weak correlations between the two order parameters signify a nonclassical crystallization pathway where the interplay between nanocrystal shape and interaction at different densities gives rise to complex assembly dynamics. Remarkably, our simulation reproduced the nonclassical nature of the experimental self-assembly pathway (Fig. 2c,e). The symmetry transitions were further analyzed by calculating lattice angle distributions (Fig. 2f)[33,35,53,54]. From 10 to 40 s, two peaks near 60° and 120° were found, which indicates a hexagonal lattice. Afterward, the distributions shifted gradually toward 70° as the system evolved into the RB phase (Fig. 2f,g). The appearance of a shoulder next to the first peak in the pair distribution function $g(r)$ provides further evidence of the hexagonal-to-RB transition (Supplementary Fig. 8). The average nearest-neighbor distance gradually increased in the early stage, probably due to charge accumulation, and later stabilized as the system transitioned into the RB phase with increasing density (Fig. 2h). Intriguingly, AuNCs at twin boundaries can collectively rotate while maintaining high local translational order, which allowed the boundary to readily propagate through misaligned grains (Fig. 2i,j, Supplementary Fig. 9 and Supplementary Movie 5). We attribute this twin-boundary migration mode to the favorable energetics of facet alignment between adjacent AuNCs, which is reproduced in simulations (Fig. 2k). The ability to resolve boundaries through cooperative rearrangement of AuNCs during

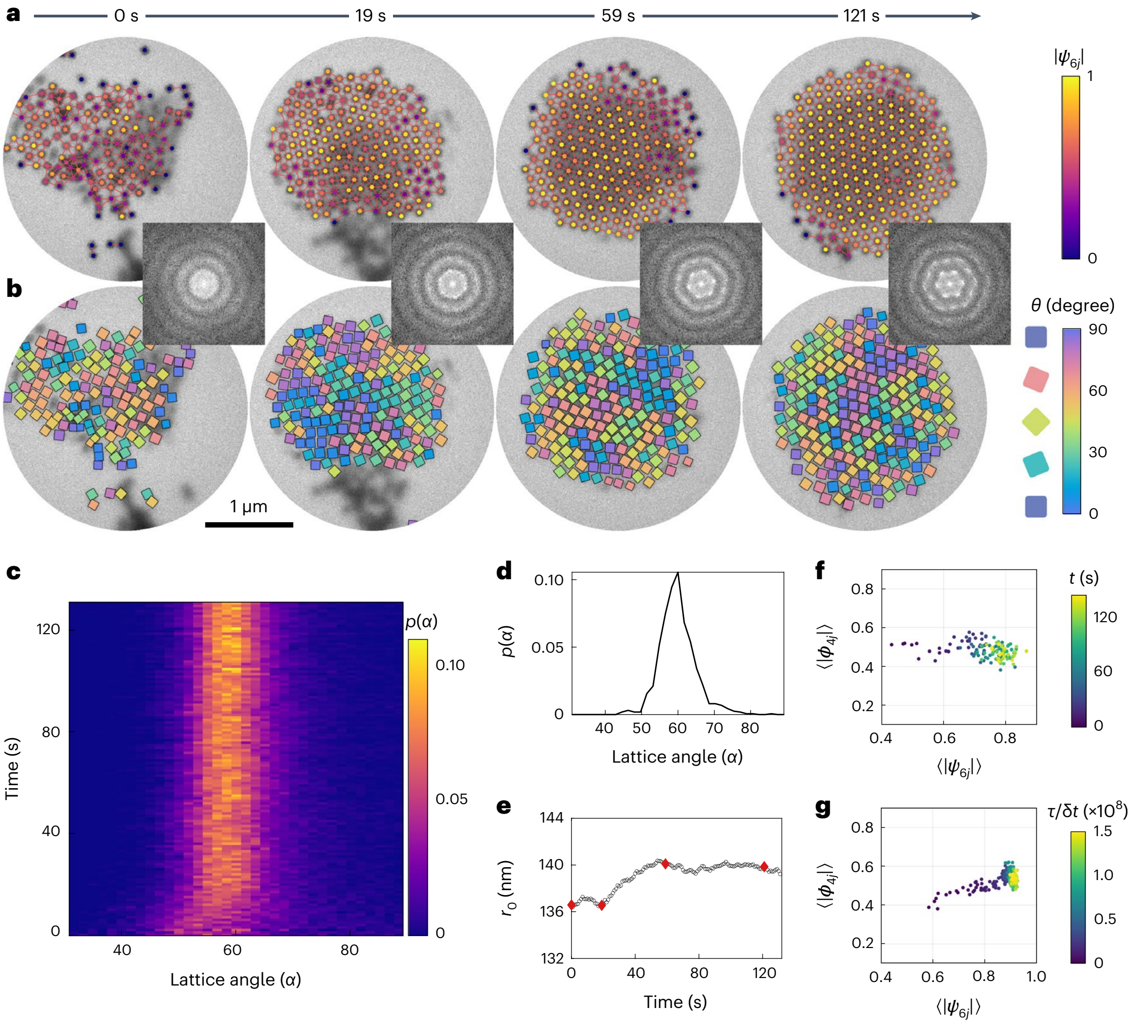

Fig. 3 | Self-assembly pathway of gold nanocubes into the HR lattice. **a**,**b**, Time-lapse LCTEM images and corresponding FFT patterns with nanocube centroids colored according to $|\psi_{6j}|$ (**a**) and nanocubes colored according to their orientations (**b**). **c**, Time-dependent lattice angle distribution. **d**, Plot of lattice angle distribution of the HR phase at $t = 121$ s. **e**, Plot of nearest-neighbor distance retrieved from the first peak of $g(r)$ versus time. The red dots highlight the four stages shown in **a** and **b**. **f**,**g**, Plots of averaged local translational and orientational order parameters ($\langle|\psi_{6j}|\rangle$, $\langle|\phi_{4j}|\rangle$) versus time from LCTEM (**f**) and simulation (**g**) data.

disorder-to-order transitions facilitates the formation of a single-crystalline RB superlattice.

The development of translational and orientational order during crystallization of the HR phase displayed a distinct pathway from the RB phase (Fig. 3 and Supplementary Movie 6). From 0 to 19 s, AuNCs assembled into a single domain consisting of a few hexagonally ordered subregions (Fig. 3a). These hexagonal regions continued to grow over the next 100 s to yield a coherent hexagonal superlattice, as illustrated by the transition from diffuse rings into sharp diffraction spots on the FFT patterns. Notably, orientational correlations among AuNCs remained short-ranged even after long-range translational order had developed, signifying the formation of a HR phase free of twin boundaries (Fig. 3b). The lattice angle distribution stayed narrowly distributed with the average close to 60° throughout the assembly process (Fig. 3c,d). The mean nearest-neighbor distance stabilized at around 140 nm after the initial rise (Fig. 3e). Notably, this value exceeds the circumdiameter of AuNCs suggesting that they can rotate freely. The decoupling of orientational and translational order was further quantified through analysis of the order parameters $\langle|\psi_{6j}|\rangle$ and $\langle|\phi_{4j}|\rangle$ (Fig. 3f and Supplementary Fig. 10). As $|\psi_{6j}|$ gradually increased and narrowed, $|\phi_{4j}|$ remained widely distributed with $\langle|\phi_{4j}|\rangle \approx 0.5$, confirming the low orientational order observed visually. The HR phase remained intact for several minutes under electron-beam illumination, suggesting that it is the stable phase under such conditions. The simulation at $(Q, \lambda) = (350\ e^-, 12\ \mathrm{nm})$ uncovered a similar kinetic pathway featuring decoupled evolution of translational and orientational order (Fig. 3g). This agreement indicates that our CG model captures the underlying physics of the experimental system.

We further examined the assembly pathway of AuNCs in high-polarity solvent (Fig. 4 and Supplementary Movie 7). Here, we used ψ_{4j} rather than ψ_{6j} to analyze local translational order, as ψ_{4j} better quantifies the SQ order observed experimentally (Fig. 4a)[54]. From 0 to 39 s, an extended network of SQ domains developed as AuNCs diffused and interacted with each other. At 119 s, a single grain consisting of extended SQ subdomains had formed, as indicated by four sets of wide FFT peaks separated by ~90°. From 119 to 269 s, SQ regions continued to enlarge resulting in narrower Bragg peaks in the FFT pattern. The lattice angles initially exhibited bimodal distributions and later merged into a single broad distribution centered at about 90° (Fig. 4c,d). Importantly, many lattice angles close to 90° were already seen at ~40 s, suggesting that there existed a tendency to maximize local facet alignment among AuNCs since the early stage of assembly. The temporal evolution of

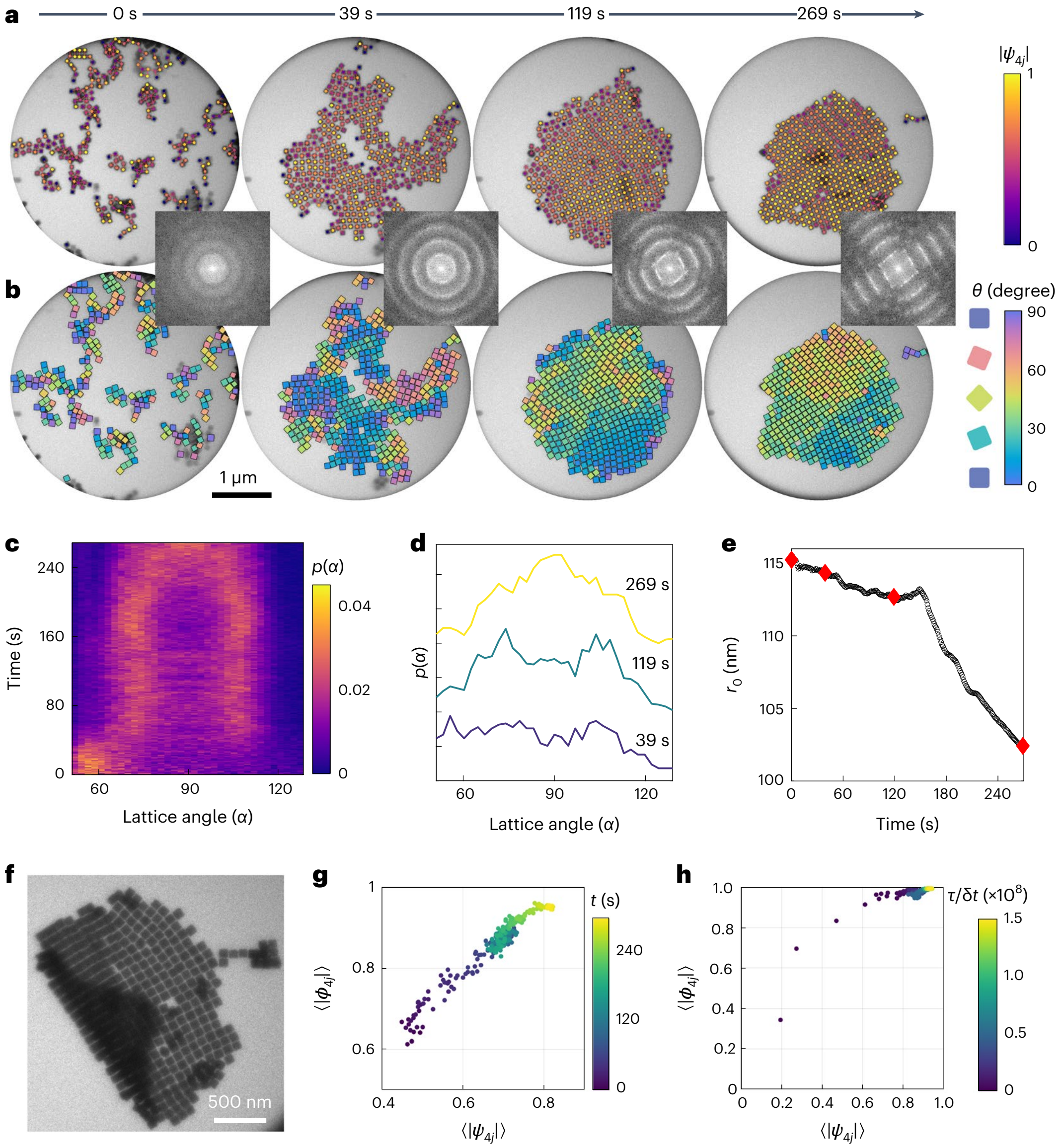

Fig. 4 | Self-assembly pathway of gold nanocubes into the SQ lattice. **a**,**b**, Time-lapse LCTEM images and corresponding FFT patterns with nanocube centroids colored according to $|\psi_{4j}|$ (**a**) and nanocubes colored according to their orientations (**b**). **c**, Time-dependent lattice angle distribution. **d**, Plots of lattice angle distribution corresponding to the final three LCTEM images in **a** and **b**. **e**, Plot of nearest-neighbor distance retrieved from the first peak of $g(r)$ versus time. The red dots highlight the four stages shown in **a** and **b**. **f**, LCTEM image showing the detachment of the SQ nanocube superlattice from the Si_3N_4 window after prolonged exposure to the electron beam. **g**,**h**, Plots of averaged local translational and orientational order parameters order parameters ($\langle|\psi_{6j}|\rangle$, $\langle|\phi_{4j}|\rangle$) versus time for LCTEM (**g**) and simulation (**h**) trajectories.

$g(r)$ reveals the development of long-range SQ order as high-order peaks gradually intensified (Supplementary Fig. 11). The average nearest-neighbor spacing monotonically decreased during assembly and reached ~102 nm at 269 s (Fig. 4e). AuNC rotation became restricted at this short distance and the superlattice continued to densify owing to strong interparticle attraction. Eventually, the superlattice membrane peeled away from the Si_3N_4 window (Fig. 4f, Supplementary Fig. 12 and Supplementary Movie 8), which is indicative of the mechanical strength provided by the strong vdW attraction and possibly the onset of polymer brush interpenetration at short distances. Distinct from the RB and HR phases, $\langle|\phi_{4j}|\rangle$ and $\langle|\psi_{4j}|\rangle$ increased concurrently and their distributions gradually narrowed during crystallization (Fig. 4g and Supplementary Fig. 11). Such enhanced coupling between translational and orientational order, which is reproduced by simulation (Fig. 4h), is attributed to strong attraction between AuNCs in high-polarity solvent and explains the absence of a ‘square rotator’ phase.

The dynamic nature of the superlattices allowed visualization of defect generation and migration. For all three phases, rows of AuNCs collectively shifted along the symmetry axes of the lattice to fill vacancies (Supplementary Figs. 13–15 and Supplementary Movie 9), as also observed in simulations (Supplementary Movies 1–3). Further, the experimental SQ lattice displayed vacancy generation and migration via a hopping mechanism. Here, vacancies formed spontaneously and translated stepwise along the symmetry axes of the lattice, occasionally oscillating between neighboring lattice sites, and vanished after reaching the periphery (Supplementary Fig. 13 and Supplementary Movie 9). This hopping mode resulted in lower vacancy mobilities compared with the RB and HR phase, indicating stronger net attractions between AuNCs forming the SQ phase[55]. Altogether, the similarities between experiment and simulation demonstrate that the interactions between AuNCs play a key role in controlling not only assembly pathways but also the defect dynamics within the superlattices.

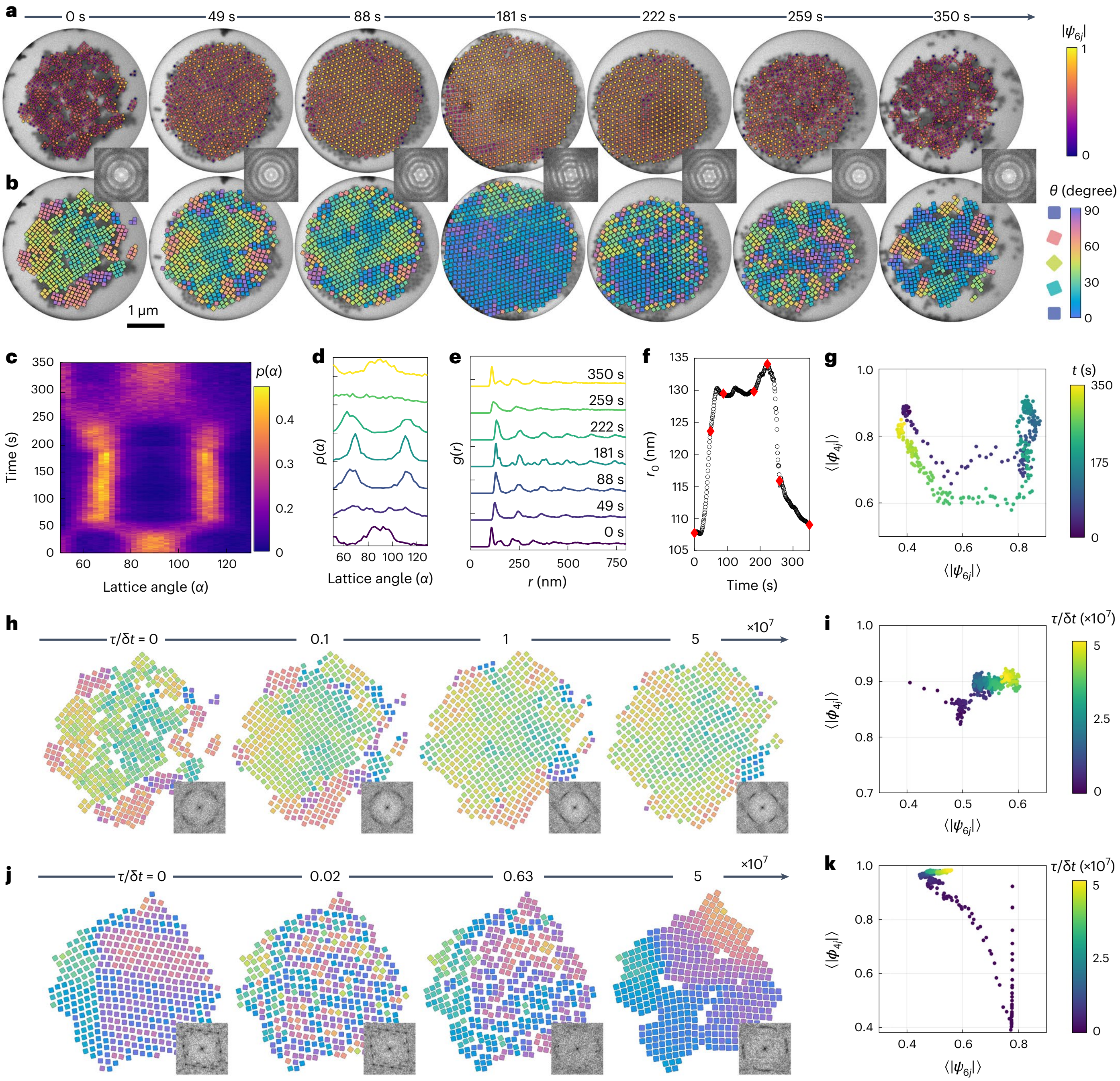

Fig. 5 | Solvent-mediated, reversible structural transitions between the SQ and the RB phases. **a**,**b**, Time-lapse LCTEM images and corresponding FFT patterns with nanocube centroids colored according to $|\psi_{6j}|$ (**a**) and nanocubes colored according to their orientations (**b**). **c**, Time-dependent lattice angle distribution. **d**,**e**, Plots of lattice angle distribution (**d**) and $g(r)$ (**e**) corresponding to the LCTEM images in **a** and **b**. **f**, Plot of nearest-neighbor distance retrieved from the first peak of $g(r)$ versus time. The red dots highlight the seven snapshots shown in **a** and **b**. **g**, Plot of averaged local order parameters ($\langle|\psi_{6j}|\rangle$, $\langle|\phi_{4j}|\rangle$) versus time for the LCTEM trajectory. **h**–**k**, Simulation snapshots with inset FFT patterns (**h** and **j**) and corresponding plots of averaged local translational and orientational order parameters ($\langle|\psi_{6j}|\rangle$, $\langle|\phi_{4j}|\rangle$) versus time for the SQ-to-RB lattice transition (**h** and **i**) and vice versa (**j** and **k**).

Solvent-mediated structural transitions between distinct superlattices

Having elucidated the self-assembly pathways of AuNCs in different solvents, we further explored superlattice reconfiguration with LCTEM and simulations. Starting from a multi-grain SQ lattice formed in butanol, we triggered its reconfiguration by quickly changing the solvent to a medium-polarity one (octane:butanol 1:1 (v/v)) and later back to butanol (Fig. 5, Supplementary Figs. 16 and 17 and Supplementary Movie 10). An extended RB superlattice emerged as indicated by the sharp spots in the FFT pattern, which subsequently returned to the polycrystalline SQ lattice (Fig. 5a,b). Lattice angle analyses revealed a fast switch from single broad distributions centered at 90° to bimodal distributions at ~50 s, which is consistent with the development of multiple RB domains as seen from LCTEM (Fig. 5c,d). Analysis of $g(r)$ provided further evidence of the SQ-to-RB transition by showing that the nearest-neighbor distance gradually increased as the RB lattice was forming (Fig. 5e,f). Initially, $\langle|\phi_{4j}|\rangle$ decreased while $\langle|\psi_{6j}|\rangle$ increased. Afterward, $\langle|\phi_{4j}|\rangle$ essentially plateaued and $\langle|\psi_{6j}|\rangle$ continued to rise followed by a steep increase in $\langle|\phi_{4j}|\rangle$ (Fig. 5g). Despite different starting states, the pathway after the initial drop in $\langle|\phi_{4j}|\rangle$ showed good agreement with that of the RB lattice formation from disorder (cf. Fig. 2c). We observed a similar but less pronounced initial decrease in $\langle|\phi_{4j}|\rangle$ in simulation, after which $\langle|\phi_{4j}|\rangle$ and $\langle|\psi_{6j}|\rangle$ increased simultaneously (Fig. 5h,i and Supplementary Movie 11). The RB-to-SQ transition, on the other hand, involved a HR-like intermediate. After solvent replacement at ~180 s, we observed a rapid decline in orientational order before the loss of lattice translational order (Fig. 5f,g), as also found in the RB-to-SQ simulation (Fig. 5j,k and Supplementary Movie 12). The appearance of HR-like intermediates probably arises from a smaller effective size of AuNCs and, hence, local particle density upon changing to a more polar solvent (Fig. 1c). The enhanced AuNC rotational freedom apparently facilitated subsequent transition to the SQ lattice. A similar fast drop in orientational order was also observed during melting of the RB lattice (Supplementary Figs. 18 and 19 and Supplementary Movie 13), which we attribute to the more isotropic and weakened interactions after switching to the low-polarity solvent (Supplementary Fig. 2). Occasionally, we also observed a different pathway for the RB-to-SQ transition in LCTEM that involved lattice distortion through collective rotation of AuNCs (Supplementary Fig. 20 and Supplementary Movie 14). The actual pathway that the system selects may depend on the local density of AuNCs and concentration of vacancies, with denser and defect-free grains probably favoring a diffusionless pathway. The solvent-mediated transitions between the SQ and RB phases appeared to be reversible based upon the nearly overlapping U-shaped trajectory of the system in $(\langle|\psi_{6j}|\rangle, \langle|\phi_{4j}|\rangle)$ space (Fig. 5g).

Discussion

In this work, we demonstrate a versatile strategy to engineer self-assembly pathways for shape-anisotropic nanoparticles while visualizing the complete assembly process using LCTEM imaging. By controlling the solvent environment, we were able to direct the formation of a HR phase with translational order but orientational disorder for weakly attractive AuNCs, and RB and SQ phases from increasingly attractive AuNCs. Using MD simulations and scaling theory, we showed that the balance between vdW attraction and electrostatic repulsion in different solvents controls superlattice formation. In both LCTEM and simulation, the evolution of lattice translational order and particle orientational order were largely decoupled during the assembly of the HR phase and strongly coupled during the assembly of the SQ phase, whereas the degree of coupling varied at different stages of the assembly process of the RB phase. Next, we expanded the capability of LCTEM to study solid–solid transitions triggered by in situ rapid solvent exchange. We observed a HR-like intermediate during the RB-to-SQ transition, and our simulations illustrated that the decreased effective particle size due to the change in electrostatic screening facilitates the formation of this intermediate. The agreement between theory, simulation and experiment provides a robust, predictive framework for understanding and manipulating assembly pathways, and we expect our findings to be applicable to a wide variety of nanocolloidal systems, regardless of the origin of their interactions. Our joint experiment–simulation–theory study thereby opens new avenues for the bottom-up design of responsive and adaptive materials-on-demand by engineering the building block attributes, kinetic assembly pathways and superlattice structure in self-assembling nanocolloids.

Methods

Computational model of AuNC and MD simulations

We modeled the AuNCs as a 2D rigid body of point particles by discretizing the particles into two types of interaction sites: a series of sites around the perimeter of the body that interact through a Yukawa potential and a grid of sites that span the body of the particle and interact through a Mie potential. The Yukawa and Mie potentials represent the screened electrostatic and Au–Au vdW interactions, respectively. MD simulations were executed with HOOMD-Blue[56]. Further details of the model parameterization and MD simulations are provided in Supplementary Note 1.

Synthesis and characterization of polystyrene-grafted AuNCs

AuNCs were synthesized via iterative reductive growth and oxidative dissolution reactions based on a previously reported method with modifications[57]. To prepare polystyrene-grafted AuNCs, 0.5 ml of the pristine AuNC solution was first concentrated to ~100 µl via centrifugation at 1,540 × *g* for 3 min. Next, this concentrated solution was added dropwise into a 10 ml tetrahydrofuran (THF) solution (2 mg ml^{-1}) of thiol-terminated polystyrene (M_w = 3.2 kDa) under sonication. The resultant mixture was left undisturbed for 24 h at room temperature. Afterward, the polystyrene-grafted AuNCs were purified via three rounds of centrifugation at 2,740 × *g* for 3 min, each time followed by redispersion into 3 ml of THF. After the last centrifugation step, the polystyrene-grafted AuNCs were dispersed in 200 µl of THF for LCTEM experiments. Low-magnification TEM images were recorded on a JEOL JEM-1400plus electron microscope with a LaB_6 filament operating at 120 kV. TEM samples were prepared by drop-casting ~10 µl of AuNC solution onto 300-mesh carbon-coated copper grids (Ted Pella). Scanning electron microscopy (SEM) images were taken on a Carl Zeiss Auriga 60 FIB-SEM operated at 1.50 kV. Further details on nanocrystal synthesis are provided in Supplementary Note 5.

In situ LCTEM imaging

In situ LCTEM imaging was performed on a JEOL JEM-1400plus electron microscope using a Protochips Poseidon Select holder. Bottom E-chips with a 150 nm integrated gold spacer (EPB-52DF-10) and top E-chips with the nominal window dimension of 550 µm × 20 µm (EPT-52W-10) were used in all experiments. LCTEM movies were recorded by a Gatan OneView CMOS camera with 4096 × 4096 pixels at a frame rate of 5 fps. Further details on LCTEM imaging and image processing and analysis are provided in Supplementary Notes 8–10.

Data availability

The source data for the figures in the main text are available in Supplementary Information.

References

1. Libbrecht, K. G. The physics of snow crystals. *Rep. Prog. Phys.* **68**, 855–895 (2005).
2. Sauter, A. et al. Real-time observation of nonclassical protein crystallization kinetics. *J. Am. Chem. Soc.* **137**, 1485–1491 (2015).
3. Pogatscher, S. et al. Solid–solid phase transitions via melting in metals. *Nat. Commun.* **7**, 11113 (2016).
4. De Yoreo, J. J. et al. Crystallization by particle attachment in synthetic, biogenic, and geologic environments. *Science* **349**, aaa6760 (2015).
5. Boles, M. A., Engel, M. & Talapin, D. V. Self-assembly of colloidal nanocrystals: from intricate structures to functional materials. *Chem. Rev.* **116**, 11220–11289 (2016).
6. Li, B., Zhou, D. & Han, Y. Assembly and phase transitions of colloidal crystals. *Nat. Rev. Mater.* **1**, 15011 (2016).
7. Ye, X. et al. Competition of shape and interaction patchiness for self-assembling nanoplates. *Nat. Chem.* **5**, 466–473 (2013).
8. Choi, J.-H. et al. Exploiting the colloidal nanocrystal library to construct electronic devices. *Science* **352**, 205–208 (2016).
9. Liu, W. et al. Diamond family of nanoparticle superlattices. *Science* **351**, 582–586 (2016).
10. Lin, H. et al. Clathrate colloidal crystals. *Science* **355**, 931–935 (2017).
11. Nagaoka, Y. et al. Superstructures generated from truncated tetrahedral quantum dots. *Nature* **561**, 378–382 (2018).
12. Alberstein, R., Suzuki, Y., Paesani, F. & Tezcan, F. A. Engineering the entropy-driven free-energy landscape of a dynamic nanoporous protein assembly. *Nat. Chem.* **10**, 732–739 (2018).

13. Bian, T. et al. Electrostatic co-assembly of nanoparticles with oppositely charged small molecules into static and dynamic superstructures. *Nat. Chem.* **13**, 940–949 (2021).
14. Santos, P. J. et al. Macroscopic materials assembled from nanoparticle superlattices. *Nature* **591**, 586–591 (2021).
15. Li, Z., Fan, Q. & Yin, Y. Colloidal self-assembly approaches to smart nanostructured materials. *Chem. Rev.* **122**, 4976–5067 (2022).
16. Coropceanu, I. et al. Self-assembly of nanocrystals into strongly electronically coupled all-inorganic supercrystals. *Science* **375**, 1422–1426 (2022).
17. Wang, Y. et al. Structural diversity in dimension-controlled assemblies of tetrahedral gold nanocrystals. *J. Am. Chem. Soc.* **144**, 13538–13546 (2022).
18. Han, H. et al. Multiscale hierarchical structures from a nanocluster mesophase. *Nat. Mater.* **21**, 518–525 (2022).
19. Kumar, P. et al. Photonically active bowtie nanoassemblies with chirality continuum. *Nature* **615**, 418–424 (2023).
20. Wang, Y. et al. Controlled self-assembly of gold nanotetrahedra into quasicrystals and complex periodic supracrystals. *J. Am. Chem. Soc.* **145**, 17902–17911 (2023).
21. Nguyen, Q. N. et al. Colloidal synthesis of metal nanocrystals: from asymmetrical growth to symmetry breaking. *Chem. Rev.* **123**, 3693–3760 (2023).
22. Silvera Batista, C. A., Larson, R. G. & Kotov, N. A. Nonadditivity of nanoparticle interactions. *Science* **350**, 1242477 (2015).
23. Král, P. et al. Simulation methods for self-assembling nanoparticles. *Prog. Mater. Sci.* **142**, 101225 (2024).
24. Waltmann, T., Waltmann, C., Horst, N. & Travesset, A. Many body effects and icosahedral order in superlattice self-assembly. *J. Am. Chem. Soc.* **140**, 8236–8245 (2018).
25. Lee, S., Teich, E. G., Engel, M. & Glotzer, S. C. Entropic colloidal crystallization pathways via fluid–fluid transitions and multidimensional prenucleation motifs. *Proc. Natl. Acad. Sci. USA* **116**, 14843–14851 (2019).
26. Zhang, T. H. & Liu, X. Y. How does a transient amorphous precursor template crystallization. *J. Am. Chem. Soc.* **129**, 13520–13526 (2007).
27. Savage, J. R. & Dinsmore, A. D. Experimental evidence for two-step nucleation in colloidal crystallization. *Phys. Rev. Lett.* **102**, 198302 (2009).
28. Peng, Y. et al. Two-step nucleation mechanism in solid–solid phase transitions. *Nat. Mater.* **14**, 101–108 (2015).
29. Ou, Z. et al. Kinetic pathways of crystallization at the nanoscale. *Nat. Mater.* **19**, 450–455 (2020).
30. Zhong, Y. et al. Multistep crystallization of dynamic nanoparticle superlattices in nonaqueous solutions. *J. Am. Chem. Soc.* **144**, 14915–14922 (2022).
31. Leunissen, M. E. et al. Ionic colloidal crystals of oppositely charged particles. *Nature* **437**, 235–240 (2005).
32. Sacanna, S., Irvine, W. T. M., Chaikin, P. M. & Pine, D. J. Lock and key colloids. *Nature* **464**, 575–578 (2010).
33. Zhao, K., Bruinsma, R. & Mason, T. G. Entropic crystal–crystal transitions of Brownian squares. *Proc. Natl Acad. Sci. USA* **108**, 2684–2687 (2011).
34. Shah, A. A. et al. Actuation of shape-memory colloidal fibres of Janus ellipsoids. *Nat. Mater.* **14**, 117–124 (2015).
35. Rossi, L. et al. Shape-sensitive crystallization in colloidal superball fluids. *Proc. Natl Acad. Sci. USA* **112**, 5286–5290 (2015).
36. Liao, H.-G. et al. Facet development during platinum nanocube growth. *Science* **345**, 916–919 (2014).
37. Ross, F. M. Opportunities and challenges in liquid cell electron microscopy. *Science* **350**, aaa9886 (2015).
38. Ye, X. et al. Single-particle mapping of nonequilibrium nanocrystal transformations. *Science* **354**, 874–877 (2016).
39. Sutter, E. et al. In situ microscopy of the self-assembly of branched nanocrystals in solution. *Nat. Commun.* **7**, 11213 (2016).
40. Lin, G. et al. Linker-mediated self-assembly dynamics of charged nanoparticles. *ACS Nano* **10**, 7443–7450 (2016).
41. Loh, N. D. et al. Multistep nucleation of nanocrystals in aqueous solution. *Nat. Chem.* **9**, 77–82 (2017).
42. Tan, S. F. et al. Nanoparticle interactions guided by shape-dependent hydrophobic forces. *Adv. Mater.* **30**, 1707077 (2018).
43. Ianiro, A. et al. Liquid–liquid phase separation during amphiphilic self-assembly. *Nat. Chem.* **11**, 320–328 (2019).
44. Song, M. et al. Oriented attachment induces fivefold twins by forming and decomposing high-energy grain boundaries. *Science* **367**, 40–45 (2020).
45. Kim, B. H. et al. Critical differences in 3D atomic structure of individual ligand-protected nanocrystals in solution. *Science* **368**, 60–67 (2020).
46. Yang, Y. et al. Operando studies reveal active Cu nanograins for CO_2 electroreduction. *Nature* **614**, 262–269 (2023).
47. Woehl, T. J. & Prozorov, T. The mechanisms for nanoparticle surface diffusion and chain self-assembly determined from real-time nanoscale kinetics in liquid. *J. Phys. Chem. C* **119**, 21261–21269 (2015).
48. Zheng, H., Mirsaidov, U. M., Wang, L.-W. & Matsudaira, P. Electron beam manipulation of nanoparticles. *Nano Lett.* **12**, 5644–5648 (2012).
49. White, E. R., Mecklenburg, M., Shevitski, B., Singer, S. B. & Regan, B. C. Charged nanoparticle dynamics in water induced by scanning transmission electron microscopy. *Langmuir* **28**, 3695–3698 (2012).
50. Woehl, T. J. et al. Experimental procedures to mitigate electron beam induced artifacts during in situ fluid imaging of nanomaterials. *Ultramicroscopy* **127**, 53–63 (2013).
51. Liu, Y., Lin, X. M., Sun, Y. & Rajh, T. In situ visualization of self-assembly of charged gold nanoparticles. *J. Am. Chem. Soc.* **135**, 3764–3767 (2013).
52. Chee, S. W. et al. Desorption-mediated motion of nanoparticles at the liquid–solid interface. *J. Phys. Chem. C* **120**, 20462–20470 (2016).
53. Avendaño, C. & Escobedo, F. A. Phase behavior of rounded hard-squares. *Soft Matter* **8**, 4675–4681 (2012).
54. Meijer, J.-M. et al. Convectively assembled monolayers of colloidal cubes: evidence of optimal packings. *Langmuir* **35**, 4946–4955 (2019).
55. van der Meer, B. et al. Revealing a vacancy analog of the crowdion interstitial in simple cubic crystals. *Phys. Rev. Lett.* **121**, 258001 (2018).
56. Anderson, J. A., Glaser, J. & Glotzer, S. C. Hoomd-blue: a Python package for high-performance molecular dynamics and hard particle Monte Carlo simulations. *Comput. Mater. Sci.* **173**, 109363 (2020).
57. O'Brien, M. N., Jones, M. R., Brown, K. A. & Mirkin, C. A. Universal noble metal nanoparticle seeds realized through iterative reductive growth and oxidative dissolution reactions. *J. Am. Chem. Soc.* **136**, 7603–7606 (2014).

Acknowledgements

X.Y. acknowledge support from the US National Science Foundation under grant numbers DMR-2102526 (nanocrystal synthesis) and CBET-2223453 (LCTEM imaging and data analysis). The theory, modeling and simulation work was supported by a CDS&E grant from the National Science Foundation (NSF), Division of Materials Research award no. DMR 2302470 (S.C.G.). Simulation work used NCSA Delta through allocation DMR 140129 from the Advanced Cyberinfrastructure Coordination Ecosystem: Services & Support (ACCESS) program, which is supported by National Science

Foundation grant nos. 2138259, 2138286, 2138307, 2137603 and 2138296. Computational resources and services also provided by Advanced Research Computing (ARC), a division of Information and Technology Services (ITS) at the University of Michigan, Ann Arbor. T.D. acknowledges support from the National Science Foundation Graduate Research Fellowship through grant DGE-1256260.

Authors contributions

Y.Z. and X.Y. designed the experiments. Y.Z., Y.W. and F.C. performed the experiments. Y.Z., T.C.M., T.D., A.B.-G., V.R.A., J.C. and X.Y. analyzed the experimental data. T.C.M., T.D. and S.C.G. designed the theoretical model and performed the simulations. Y.Z., T.C.M, T.D., J.C., S.C.G. and X.Y. wrote the manuscript. S.C.G. and X.Y. supervised the project. All authors discussed the results and commented on the manuscript.

Competing interests

The authors declare no competing interests.

Additional information

Supplementary information The online version contains supplementary material available at https://doi.org/10.1038/s44286-024-00102-9.

Correspondence and requests for materials should be addressed to Sharon C. Glotzer or Xingchen Ye.

Peer review information *Nature Chemical Engineering* thanks Taylor Woehl, Petra Kral and Ethayaraja Mani for their contribution to the peer review of this work.